Dynamic charge modulate lithium uniform plating functional composite anode for dendrite-free lithium metal batteries

Wendi Zhang [a], Qianxiao Fan [a], Dongmei Zhang [a], Lehao Liu [a], Shen Liu [a], Zhengyuan Fang [b], Wei Li [c], Xiaodan Li [b,*], Meicheng Li [a,*]

[a] State Key Laboratory of Alternate Electrical Power System with Renewable Energy Sources, North China Electric Power University, Beijing 102206, China
[b] Fujian Provincial Key Laboratory of Functional Materials and Applications, School of Materials Science and Engineering, Xiamen University of Technology, Xiamen 361024, China
[c] Benjamin M. Statler College of Engineering and Mineral Resources West Virginia University Morgantown, WV 26506, USA

A B S T R A C T

Lithium metal is considered as the 'sharp blade' to break through the limitation on energy density of lithium batteries. However, uneven plating of lithium metal during charge/discharge process causes serious safety hazards. Here, a carbon-based 3D skeleton (CC@Co-NCNTs) with Co nanocrystals anchored N-containing carbon nanotubes (Co-NCNTs) was constructed to induce the uniform lithium plating towards dendrite-free lithium metal batteries. The Co-NCNTs in the skeleton exhibit enhanced lithophilicity, supplying abundant nucleation sites. Moreover, the ingenious hierarchical structure reconstructs the current density distribution, promoting the uniform lithium plating. Particularly, the electrons from the Co nanocrystals are transferred to the surface of Co-NCNTs, which offers a dynamic charge distribution on the surface of the skeleton along with the plating of lithium ions during the charge-discharge process, thus modulating uniform lithium plating on the Co-NCNTs skeleton. The above-mentioned mechanism is further verified by first-principle calculations and multi-physical field simulation. Thus, the CC@Co-NCNTs@Li symmetric cell presents a long-term cyclic stability (over 1300 h) at a high current density of 40 mA cm^{-2}. The CC@Co-NCNTs@Li/LiFePO$_4$ cell still delivers a discharge capacity of 135 mAh g^{-1} at 1 C after 500 cycles. This work provides new insights to the study of functional skeletons for dendrite-free lithium batteries.

1. Introduction

Lithium metal, which meets the requirements of high energy density lithium batteries, is considered as one of the most potential anode materials [1]. The characteristics of ultra-low redox potential (-3.04 V, vs. standard hydrogen electrode) and high theoretical specific capacity (3860 mAh g^{-1}) endow it with a predominant position in the next-generation anode material [2]. However, accompanied by infinite volume changes of lithium metal, the continuous reaction between lithium and electrolyte tends to deplete the electrolyte. The uncontrollable growth of lithium dendrite during the charge-discharge process trends to induce short circuit, resulting in battery failure and even combustion. These problems extremely hinder the promoted commercial application of lithium batteries [3,4].

To achieve the practical application of lithium metal anodes, some effective strategies have been proposed to overcome the formation and growth of lithium dendrites, such as solid electrolytes [5–8], electrolyte additives [9–12], and modified SEI membrane [13–17]. However, lithium metal is a frame-less electrode which suffers huge volume change during electrochemical process. When the volume changes drastically, the protection mechanism constructed by the above strategies is unstable, thus it is difficult to continuously suppress the dendrite growth for a long time. Lithium composite anodes structured by conductive skeletons can adjust the lithium plating and suppress the volume changes, and are considered as is an ideal strategy to improve the electrochemical performance of lithium metal anodes [18]. Furthermore, considering that the mass ratio of conductive skeleton in the composite anode would reduce the energy density of electrodes, carbon materials show great potential as the conductive skeleton of lithium metal due to their good electrical conductivity, natural abundance and especially the lighter weight than metal materials (eg. Cu, Ni) [19–26]. However, the pure carbon-based host displays very faint

lithium affinity, and cannot afford uniform lithium plating/stripping [27]. The lithophilicity of carbon-based host can be improved by doping polar elements (such as N, O) and surface modifying with Ag, ZnO or other lithophilicity coatings [18,28–30]. Typically, the silver-coated carbon fiber-based composite Li anode (CF/Ag-Li) was prepared through Ag electroplating and molten Li infusion [18]. The CF/Ag-Li symmetrical cells exhibited a cyclic stability of > 400 h at 1 mA cm^{-2}. However, these methods involving in complicated process suffer from the increased undesired reaction in batteries or high cost in the time and labor. In addition, these modified carbon-based hosts are generally limited in their roles as lithium philophiles and in reduced current density, but are scarce of ingenious regulation towards lithium plating/stripping kinetics. CNT usually requires transition metal atoms (Fe, Co, Ni, etc.) as catalysts during the growth process, making the transition metal clusters anchor to the carbon nanotubes naturally. It is investigated that the Co clusters anchored on the surface of CNT can regulate the charge distribution and electron transfer properties on the skeleton of CNT by forming local dipoles [31]. This change is likely to give the ability of influencing the lithium striping and plating kinetics. Therefore, the deep exploration and application of this mechanism is critical to achieving rapid and uniform lithium plating/stripping.

In this work, we designed a 3D skeleton composed of flexible carbon fiber and hierarchical nanosheets assembled by Co nanocrystals anchored N-containing carbon nanotubes (NCNTs) networks to achieve the ultra-stable lithium dendrite-free plating/stripping performance. The results show that CC@Co-NCNTs can effectively control the high-rate and uniform lithium plating, and obviously avoid the growth of lithium dendrites through an ingenious regulation of dynamic charge distribution on its surface. The CC@Co-NCNTs@Li anode (i.e., filling Li metal in the CC@Co-NCNTs) exhibits ultra-long cycle stability and ultra-low overpotential in a symmetrical cell, stable cycling for more than 1400 h at a current density of 5 mA cm^{-2}, and a minimum voltage hysteresis of 4.3 mV. The lowest overpotential in stripping/plating behavior at a current density of 5 mA cm^{-2} with a capacity of 5 mAh cm^{-2} was firstly reported. In the full cell of CC@Co-NCNTs@Li/LiFePO$_4$, it still maintains high coulombic efficiency ($>99.9\%$) long-term cyclic stability and excellent rate performance.

2. Experimental section

2.1. Material synthesis

Preparation of CC@Co-NCNTs@Li: All reagents are analytical grade. The carbon cloth was soaked in a 1 wt% HCl solution for 10 min, and then washed with deionized water and dried for use. As previously reported, 0.197 g Zn(NO$_3$)$_2$.6 H$_2$O and 0.385 g Co(NO$_3$)$_2$.6 H$_2$O were dissolved in 40 mL of deionised water and stirred to obtain a homogeneous solution. Similarly, the other homogeneous solution was obtained by dissolving 1.3 g of dimethylimidazole in 40 mL of deionised water. The preprocessed carbon cloth was suspended in the mixture of the above two solutions, and then a quick stirring was conducted at room temperature for 4 h. after washing and drying, the carbon cloth covered with leaf-like ZnCo-Zeolitic Imidazolate Frameworks (CC@ZnCo-ZIF) was obtained. The as-prepared CC@ZnCo-ZIF was placed in a tube furnace and calcined at 600 °C for 2 h at a heating rate of 1 °C min^{-1} under the protection of N$_2$ atmosphere. The calcined product was soaked in a 1 wt% HCl solution for 2 h following by washing with deionized water to obtain CC@Co-NCNTs. The CC@Co-NCNTs was punched into wafers, and soaked in a molten metal Li (220 °C) liquid for 3 min in a glove box with argon. Finally, a composite anode of CC@Co-NCNTs and metal Li was obtained, and called as CC@Co-NCNTs@Li.

2.2. Characterization

The morphology and surface structure of the samples were obtained by scanning electron microscope (SEM, Zeiss, EVO® 18). The detailed morphology and structure were characterized by TEM and HRTEM microscopes (FEI Talos 200 s) with energy dispersive X-ray detector (EDX). The chemical composition and surface element state were characterized by XPS (ESCALAB 250Xi, Al Ka radiation). The nitrogen adsorption/desorption isotherms were performed on a 77 k Quan tachrome.

2.3. Electrochemical measurements

Symmetrical cell: The CC@Co-NCNTs@Li composites, which were used as the cathode and anode at the same time, the separator (Celgard 2000) and electrolyte (90 μL) were assembled into a CR2032 coin cell in a glove box with argon. The electrolyte was a mixture of ethylene carbonate (EC) and dimethyl carbonate (DMC) (v/v=1:1) with 1.0 M LiPF$_6$ and 5 wt% fluoroethylene carbonate (FEC). Galvanostatic charge-discharge process were carried out on a standard eight-channel battery tester (LANHE CT3002A) with a current density range of 0.5–40 mA cm^{-2}.

Full cell: The active material (LiFePO$_4$), the conductive agent (Super-P) and the binder (5 wt% PVDF) were mixed in a mass ratio of 8:1:1 and coated on the aluminum foil. Then the sample was dried at 110 °C in vacuum overnight and tailored into wafers with a diameter of 12 mm. The average mass loading of active material for each wafer was 4.0 mg cm^{-2}. Then the as-prepared LiFePO$_4$ cathode, the CC@Co-NCNTs@Li anode, the separator and the above electrolyte were assembled into a CR2032 full cell in an argon glove box. Galvanostatic charge-discharge performance of the full cells were carried out in a voltage window of 2.5–4.2 V. The impedance spectra were collected by electrochemical workstation (Autolab, PGSTAT 302 N) from 100 kHz to 0.01 Hz.

2.4. First-principles calculations

Based on density functional theory (DFT), all atoms in the structural models were optimized to the ground state using the projector augmented wave (PAW) method in the Vienna AB-Initio Simulation Package (VASP) software. The Perdew-Burke-Ernzerhof (PBE) functional under generalized gradient approximation (GGA) is adopted for the exchange-correlation functions. The value of the cut-off energy of plane wave is set to 520 eV. The original carbon nanotubes (a=9.61, b=9.61, c=4.26) with a chirality of (8,0) use a $3 \times 3 \times 6$ Monkhorst-Pack (MP) grid. The k-points for the Brillouin zones were set to $1 \times 1 \times 3$ for the expanded carbon nanotubes (a=20, b=20, c=8.53), subsequent N-doped models, and adsorption models. The relaxation of all models ends when the force on all atoms is less than 0.02 eV Å^{-1} and the electrons self-consistently converge to 1×10^{-5} eV.

2.5. Co-CNT current density simulation

We simulated the current density distribution of Co-CNTs using COMSOL Multiphysics. For comparison, the pure CNTs were also added. A typical lithium battery model was built using Co-doped carbon nanotubes (Co-CNTs) as anode and standardized LiFePO$_4$ as cathode. To simplify the model, ten Co (3 nm) particles were distributed on the surface of CNT (length: 50 nm, 5 nm internal diameter, 8 nm outer diameter) and only vertical arrangement was in consideration. Only the effect of the electrical conductivity on the battery response was investigated when Co-CNTs and CNTs were used as anodes:

$$i_s = -\sigma_s \nabla \phi_s$$

where σ_s is the electrode conductivity and $\nabla \phi_s$ is the electrode potential gradient. The conductance rates of Co-CNTs and CNTs were 8×10^4 S m^{-1} and 1.5×10^8 S m^{-1} respectively. The Li-ion behavior of the model can be described with the Nernst Planck equation:

$$N_i = -D_i \nabla c_i + \frac{z_i F}{RT} D_i c_i \nabla \phi_l$$

where N_i is the ion flux (unit: mol m^{-2} s^{-1}), D_i is the diffusion coefficient of the ion in the electrolyte (unit: m^2 s^{-1}), ∇_{ci} is the concentration gradient, $\nabla_{\phi l}$ is the potential gradient and z_i is the number of charges. The terms on the right of the equation represent ion diffusion and migration, respectively. F is Faraday constant: 96485 C mol^{-1}, R is universal gas constant: 8.3145 J mol^{-1} K^{-1} and T is system temperature: 293.15 K.

Ion diffusion in the positive and negative electrode materials adopts the Fick's rule:

$$N_{Li} = -D_{Li}\nabla c_{Li}$$

where D_{Li} is the ion diffusion coefficient in cathode and anode materials.

The Faraday's rule is used to reveal the relationship between the ion flux and the chemical reaction:

$$-n \cdot N_i = \sum_m R_{i,m}$$

$$R_i = \frac{v_i i_{loc}}{nF}$$

Where n is the ionic charged number (for Li ion the number is 1), i_{loc} is the current of the electrolyte and the electrode surface and v_i (equal to 1) is the chemical equivalents.

3. Results and discussion

The preparation process of CC@Co-NCNTs@Li composite anode was shown in Scheme 1. Co(NO$_3$)$_2$.6H$_2$O as the cobalt source and Zn(NO$_3$)$_2$.6H$_2$O as the zinc source react with dimethylimidazole as the organic ligand on the surface of carbon fiber. After the simple solution reaction, the carbon fiber cloth covered with CoZn-ZIF (CC@CoZn-ZIF) was obtained. During the calcination of CC@CoZn-ZIF, the leaf-like CoZn-ZIF on the surface of carbon fiber is transformed into the nanosheets, in which the reduced Co/Zn nanocrystals uniformly distributed. Particularly, the presence of slight Zn increases the catalytic efficiency of Co towards the growth of graphitized carbon during calcination process, resulting in the formation of interwoven carbon nanotubes [32]. After that, these Zn nanocrystals were removed under the treatment of dilute hydrochloric acid to form a N-doped carbon framework anchored with Co nanocrystals (CC@Co-NCNTs). Finally, CC@Co-NCNTs skeleton was filled with molten lithium to obtain the CC@Co-NCNTs@Li composite anode whose digital photo was shown in Figure S1. The mass percentage of lithium in the CC@Co-NCNTs@Li composite anode is 50 %.

According to the scanning electron microscope (SEM) image, the carbon cloth is composed of plentiful carbon fibers with a diameter of ~7 μm (Fig. 1a). For comparison, the CC@Co-NCNTs skeleton shows a uniform hierarchical structure in which abundant Co-NCNTs nanosheets are vertically distributed on the surface of carbon fibers. The length of each nanosheet is 1.5–2 μm, and the thickness is about 35 nm (Fig. 1b). In detail, the single Co-NCNTs nanosheet is a dense network of interwoven carbon nanotubes (Fig. 1c). Transmission electron microscopy (TEM) further revealed the structure of the Co-NCNTs nanosheet. The diameter of N-doped carbon nanotubes is about 8 nm and the length is tens of nanometers. Many Co nanocrystals (2–10 nm) are evenly dispersed inside and outside the N-doped carbon nanotubes (Fig. 1e). This can be verified by the EDX line scan and element mapping of the Co-NCNTs nanosheet. Co, N, and C elements are uniformly distributed on the nanosheet, and their trendline of the position change are consistent (Fig. 1d, S2). To further verify the existence of Co in NCNTs, high-resolution transmission electron microscopy (HRTEM) observes the lattice fringes with a pitch of 0.34 nm, which belongs to the (0 0 2) crystal plane of graphitic carbon (Fig. 1f,g). Simultaneously, the lattice fringes with 0.2 nm spacing between the crystal planes of Co metal (0 0 2) also appeared in the nanosheet, demonstrating the existence of Co nanocrystal in the Co-NCNTs nanosheet (Fig. 1 f,g).

Actually, the skeleton material with large specific surface area and porous properties is favourable for reducing the current density, which further promotes the uniform plating of lithium ions. The porosity of the CC@Co-NCNTs was studied by nitrogen adsorption/desorption isotherms. The specific surface area of CC@Co-NCNTs calculated by Brunauer-Emmett-Teller (BET) method is 37.3 m^2 g^{-1}. As shown in Fig. 2a, CC@Co-NCNTs exhibits a type IV absorption/desorption isotherm with an H4 hysteresis loop, demonstrating a porous structure with a mixture of slits and mesopores. The corresponding illustration further confirms the pore size distribution of CC@Co-NCNTs according to the Barrett-Joyner Halenda (BJH) model. The pore sizes of CC@Co-NCNTs are mainly in a range of 2–10 nm, which is derived from the gaps of the interwoven NCNTs network and stacking nanosheets. These gaps provide abundant nucleation sites for lithium plating.

With the purpose of verifying the chemical state in Co-NCNTs, the
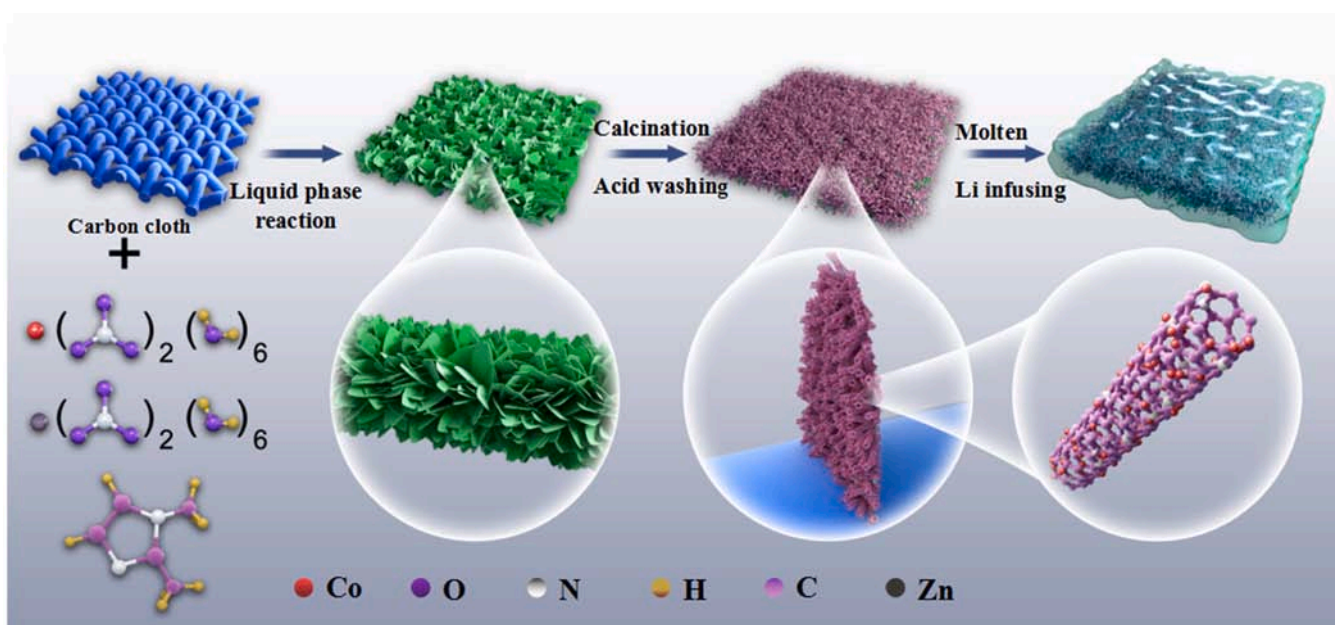
Scheme 1. Illustration of the fabrication process of CC@Co-NCNTs@Li composite anode.
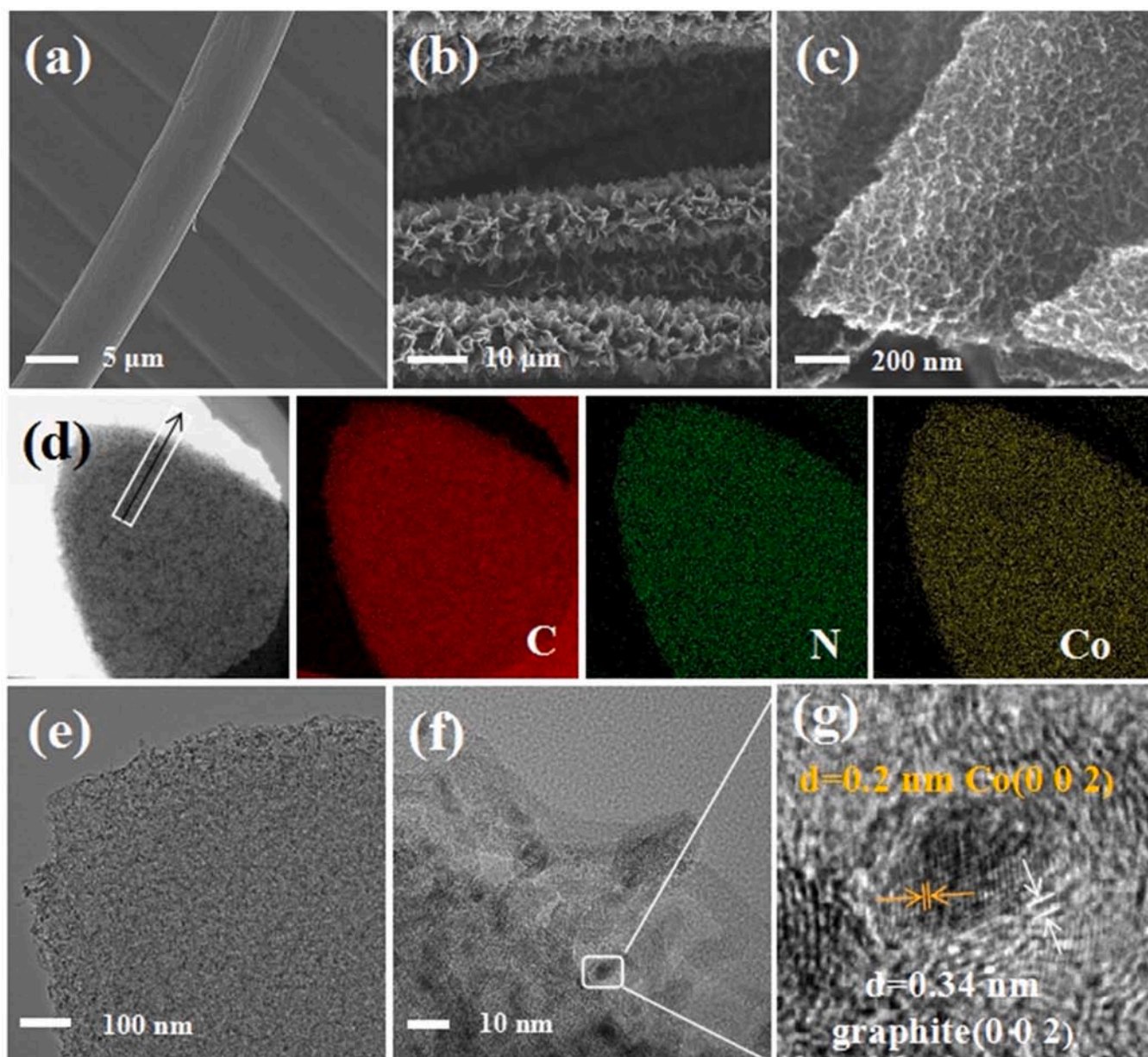
Fig. 1. Morphological characterization. a) SEM image of carbon cloth. b) SEM image of CC@Co-NCNTs. c) SEM image of Co-NCNTs nanosheet. d) HAADF image and C, Co, N element distribution of Co-NCNTs nanosheet. e) TEM image of Co-NCNTs. f,g) HRTEM image of Co-NCNTs.

chemical state of the elements on the surface of CC@Co-NCNTs was studied by X-ray photoelectron spectroscopy (XPS). In the high-resolution C 1 s spectrum (Fig. 2b), the three peaks of 284.8 eV, 285.7 eV and 288.5 eV are derived from C-C, C-N and N=C-N [33–35], respectively. The C-N bond indicates the presence of N doping, which is consistent with the analysis of N 1 s spectrum in Fig. 2c. The binding energies located at 398.1, 399.8 and 401.1 eV represent pyridine N, pyrrole N and graphite N[36,37], respectively. The corresponding contents calculated by area integral are 33 %, 34 % and 33 %. The plentiful pyrrole N and pyridine N sites could improve the lithium affinity of carbon-based skeleton [28]. The high-resolution Co 2p spectrum also shows the characteristic peaks of Co 2p 1/2 and Co 2p 3/2 (Fig. 2d). The peak of Co 2p 3/2 is deconvolved into two peaks at the binding energy of 778.2 eV and 781.2 eV corresponding to the Co metal and Co-N bond [38,39], respectively, which indicates the strong interaction between Co and NCNTs. The vigorous interaction plays a significant role in the process of lithium plating/stripping.

To gain deep insight into the effect of Co-anchoring on the surface

lithiophilicity of NCNTs, the NCNTs-based models were constructed and optimized according to density functional theory (DFT). Fig. 3a is the unit cell coordinate system of NCNTs. The different adsorption sites of Co atom on NCNTs are shown in (Fig. 3b-f). Calculated by formula (1).

$$E_{ads} = E_{total} - E_{sub} - E_{Li} \tag{1}$$

where E_{total}, E_{sub}, and E_{Li} are the energy of Li-Co-NCNT model, Co-NCNT model, and Li ion, respectively. The binding energies of Co-NCNTs are between -1.98 eV and -1.42 eV (negative values represent the adsorption process). The adsorption site shown as Fig. 3c offers the highest binding energy of -1.98 eV, which further demonstrates the strong interaction between Co and NCNTs. On this basis, the adsorption of Li on Co-NCNTs was studied. As a comparison, the binding energy of NCNT-Li was calculated. The binding energy of NCNTs and Li is -1.60 eV (Fig. 3g). However, the binding energy of Co-NCNTs and Li significantly increases to -1.98 eV due to the existence of Co atom (Fig. 3h). Especially, the binding energy of Co-NCNTs-Li sharply
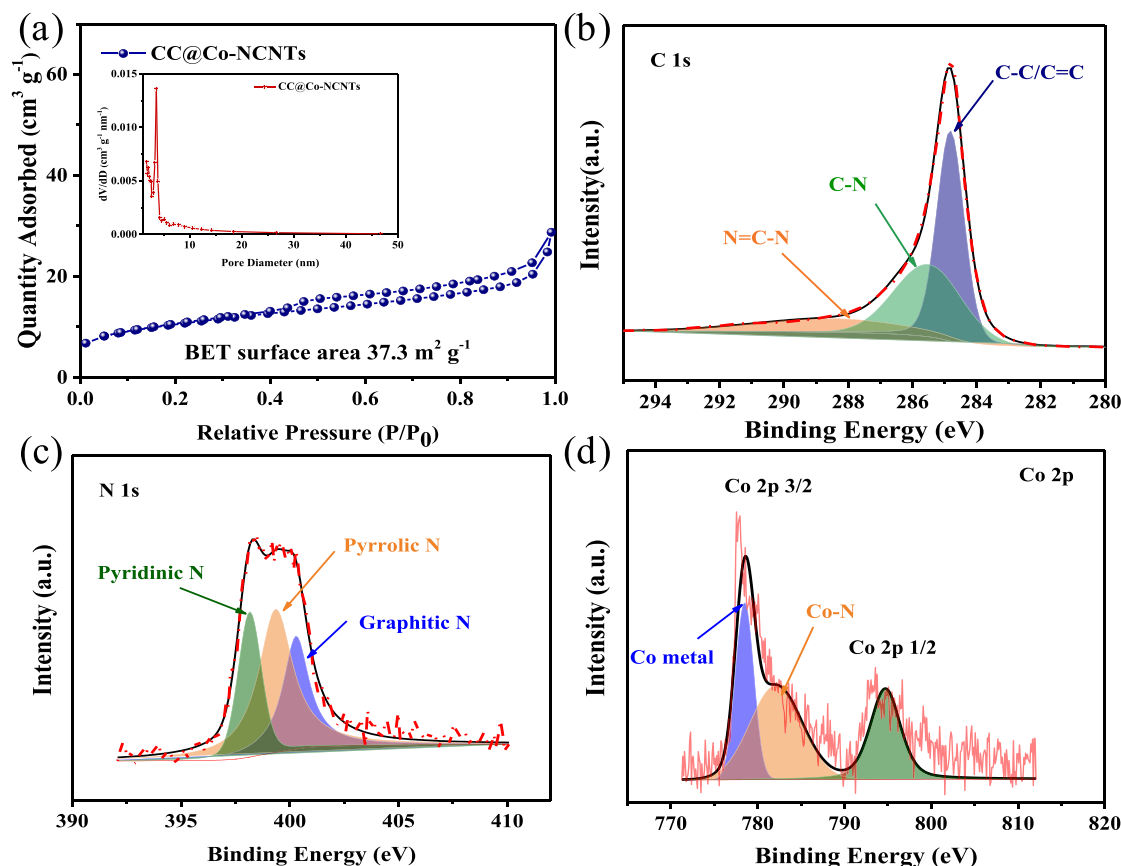
Fig. 2. a) N_2 adsorption-desorption isothermals and pore size distribution of CC@Co-NCNTs. High-resolution XPS spectra from b) C 1 s, c) N 1 s, and d) Co 2p.

increases to − 2.56 eV at the present of Co cluster (including 4 Co atoms) (Figure S3). Therefore, these Co clusters could enhance the bond of Li and carbon skeleton, ensuring the stability of Co-NCNTs-Li system to accommodate the volume expansion of electrode during charge-discharge process. To further understand the role of Co clusters in lithium plating/stripping, we calculated the charge distribution of Co-NCNTs and gave differential charge density diagrams (Fig. 3i, j), where yellow represents the charge gain region, and blue represents the charge lost region. Obviously, the surface electrons of Co clusters are transferred to Co-NCNTs, generating a charge gain region on Co-NCNTs, which helps to the adsorption of Li^+ on the surface of Co-NCNTs. Subsequently a dynamic charge distribution induces the anisotropic plating of lithium on the Co-NCNTs nanosheets, suppressing the formation of lithium dendrite during Li plating process. The detailed mechanism will be further demonstrated in the following discussion.

Furthermore, we simulated the current density distribution using COMSOL Multiphysics to further investigate the plating process of Li ions on CNTs with/without Co particles. As is depicted in the model without Co particles (Fig. 4a), the cross section on the top of CNT shows uneven current density distribution, especially the highest current density at the edges (red concentric ring). It can be concluded that the plating behavior of Li ion mainly occurs at the top regions between CNTs, and then the gaps between the carbon tubes become unavailable for lithium plating. When the top of CNTs is filled with lithium metal, lithium dendrites may tend to form locally. With the introduction of Co particles, the current density on the top region of Co-CNT becomes uniform and the surface of Co-CNTs has a significantly high current density (Fig. 4b). The abundant adsorption site for lithium ion and corresponding high current density both induce the orderly uniform plating of lithium metal, filling the gaps between Co-CNTs, and then the top region of Co-CNTs. This phenomenon is consistent with the cross section variation of carbon-lithium composite electrode before/after

cycling (Figure S6). These results further prove that the structure of Co-CNTs is beneficial to promote the uniform plating of Li ions, thus inhabiting the growth of lithium dendrites.

To evaluate the high-rate and dendrite-free lithium plating/stripping behavior driven by dynamic charge distribution on the as-prepared 3D skeleton, the galvanostatic charge-discharge cyclic performance of CC@Co-NCNTs@Li symmetric cell and bare Li symmetric cell were compared at various current densities and capacities. Fig. 5a shows the voltage distribution curves of the CC@Co-NCNTs@Li electrode and the bare Li counterparts at a current density of 5 mA cm^{-2}, with a capacity of 5 mAh cm^{-2}. The bare Li electrode shows severe asymmetry and great overpotential at the beginning of charge. The voltage hysteresis rises to 300 mV after 38 h and keeps continuous increase in the subsequent cycles. By comparison, the voltage hysteresis of the CC@Co-NCNTs@Li slightly increases at the initial stage, but drops rapidly to 30 mV after 12 h. It may be related to the integration degree between lithium metal and the skeleton. In the subsequent charge-discharge cycles, the overpotential gradually reaches to 8 mV and remains stable over 1400 h. Even at the current density of 10 mA cm^{-2} with a capacity of 10 mAh cm^{-2}, the cyclic stability of CC@Co-NCNTs@Li is up to 1000 h, and the corresponding overpotential remains at a low value of 40 mV (Figure S4) , which represents the lowest value among all the reported NCNTs@Li symmetric cells (under the same parameter). Meanwhile, the overpotential of the bare Li rapidly rises to 407 mV in 112 h, which may be due to the uneven lithium plating on the surface of bare Li. These lithium dendrites tend to fracture and fall off to form dead lithium, which in turn hinders lithium plating. Under the condition of ultrahigh current density (40 mA cm^{-2}) and stripping/plating capacity (13.3 mAh cm^{-2}) (Fig. 5b), the overpotential of bare Li rises rapidly to an alarming vaule of 2.5 V in 90 h, resulting in possible battery failure. Remarkably, the CC@Co-NCNTs@Li still presents a long-term cyclic stability of 1300 h with a low overpotential of 160 mV. The lithium plating/
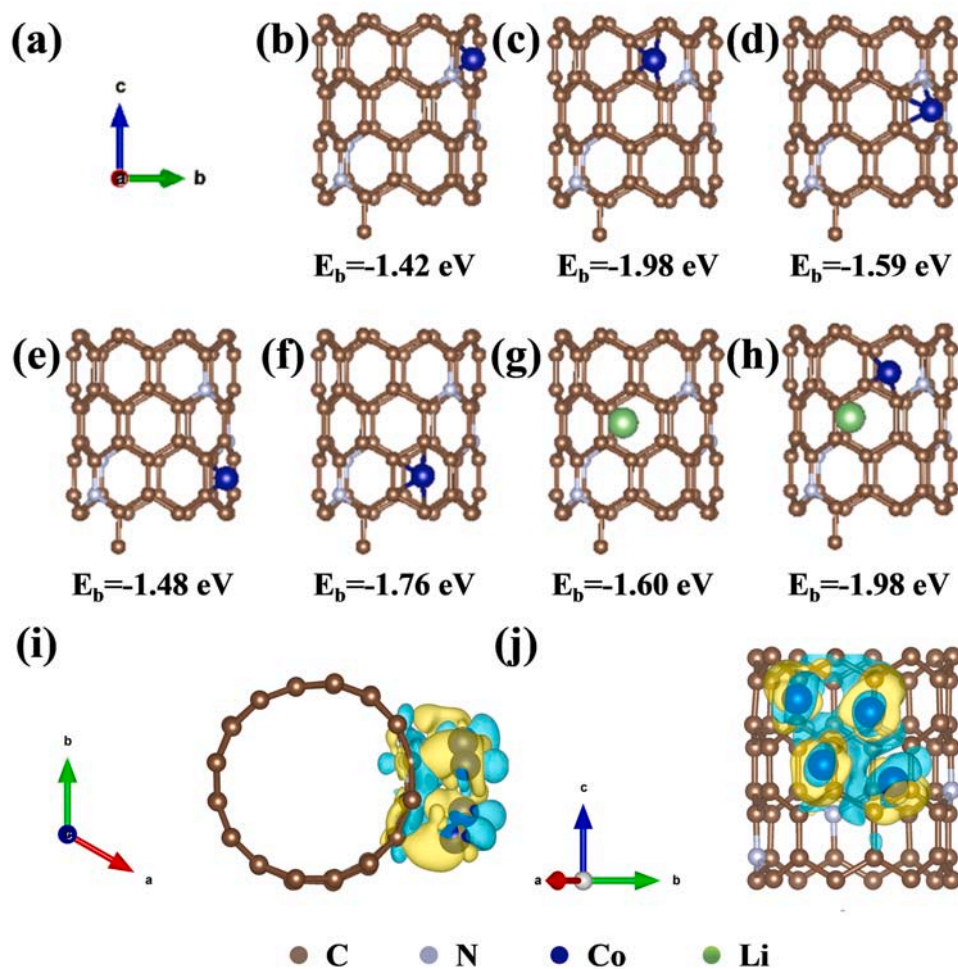
Fig. 3. Lattice structure coordinates a, b, c, d, e, f) Co atom adsorption model and adsorption energy at different sites on NCNTs. g) The adsorption model and adsorption energy of Li atoms on NCNTs. h) The adsorption model and adsorption energy of Li atoms on Co-containing NCNTs. i, j) Differential charges of Co adsorbed on NCNTs under different viewing angles.
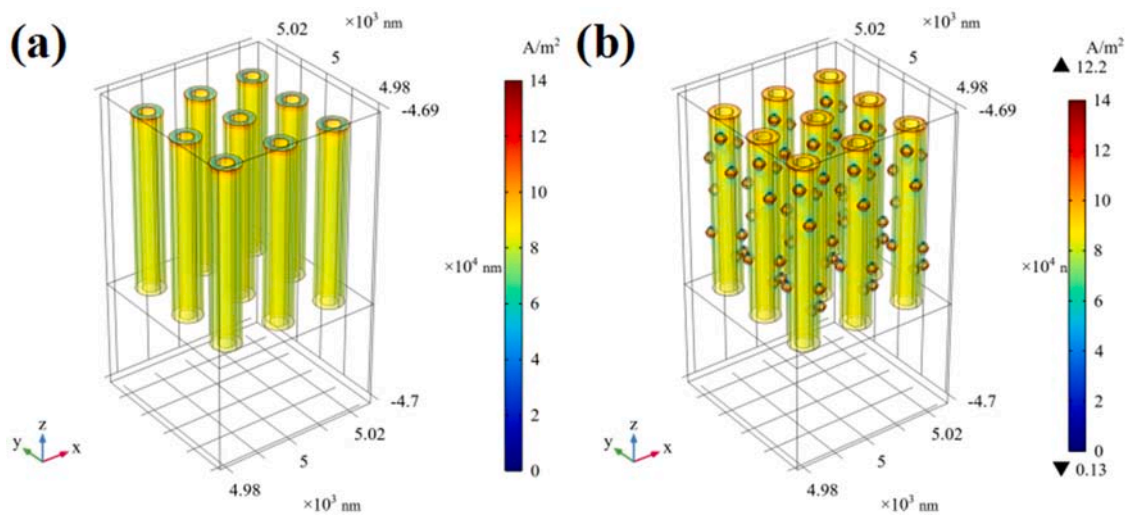

Fig. 4. Simulation results of the current density distribution of a) CNTs. b) Co-CNTs.

stripping occurs at ultra-low nucleation overpotential due to the minimized electron transfer path between the skeleton and lithium ions, which is driven from the electron aggregation on the interface modulated by dynamic charge distribution on the surface of CC@Co-NCNTs skeleton. The cyclic life of CC@Co-NCNTs@Li (1300 h) is much higher than that of previously reported Li@CNT sponge macrofilm (200 h) [40] at a current density of 40 mA. In fact, among the previous studies, cyclic stability of various composite anodes over 1000 h is rarely
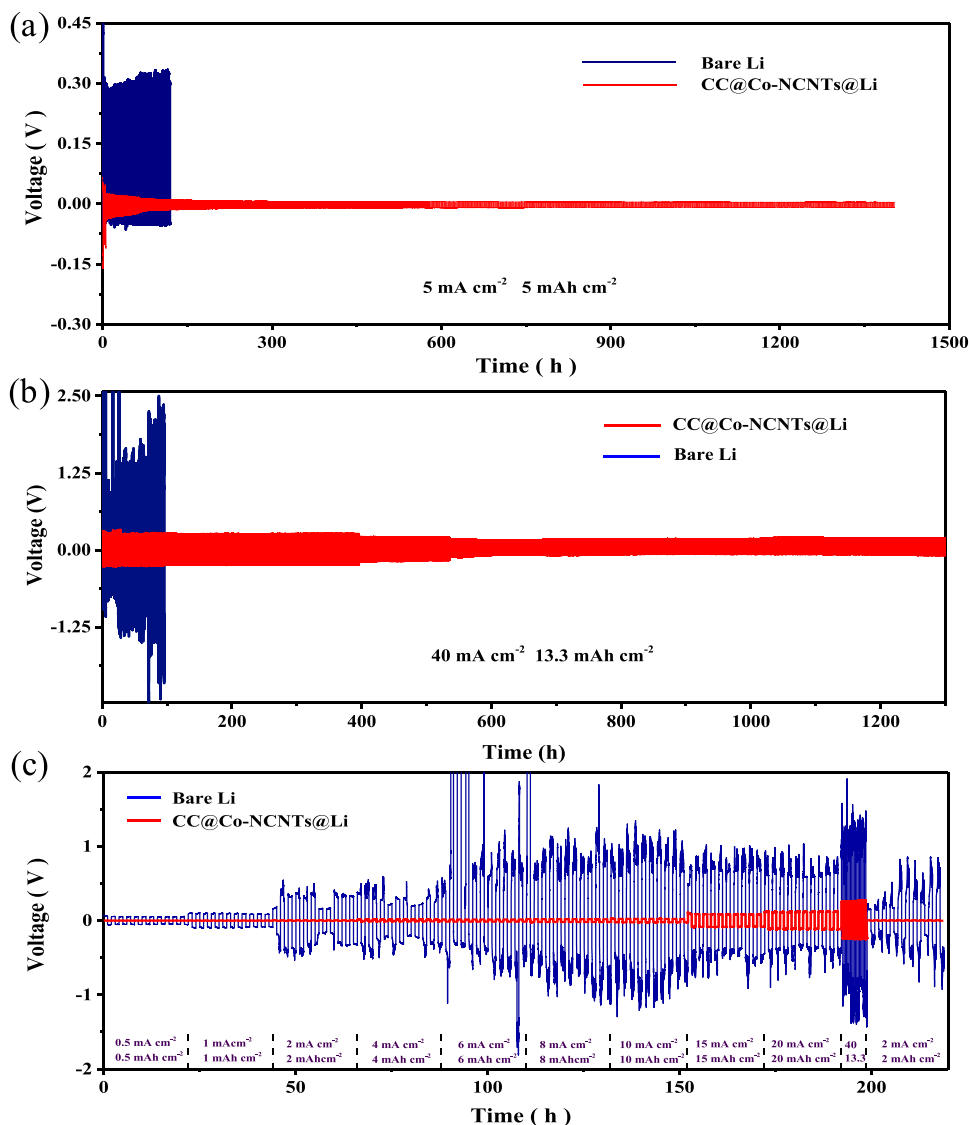
Fig. 5. The compared voltage distribution of bare Li and CC@Co-NCNTs@Li at various current densities and stripping/plating capacities. a) 5 mA cm^{-2}, 5 mAh cm^{-2} (Including a section of 0.417 mAh cm^{-2}). b) 40 mA cm^{-2}, 13.3 mAh cm^{-2}. c) 0.5–40 mA cm^{-2}, 0.5–13.3 mAh cm^{-2}.

found under high current density (Table S1).

To better analyze the Li stripping/plating behavior at high current density, Figure S5 gives an enlarged detail of the galvanostatic charge-discharge curve in Fig. 5b. The voltage distribution of the bare Li electrode shows unstable and zigzag contours, with high voltage hysteresis, while that of CC@Co-NCNTs@Li appears smooth and stable edges with slight voltage hysteresis. The good electrical conductivity and lithium philicity of 3D skeleton reduces the nucleation barrier of lithium on the surface of CC@Co-NCNTs@Li electrode. Meanwhile, the dynamic charge distribution of Co and NCNT network assists the uniform Li plating process. Thus, the overpotential of CC@Co-NCNTs@Li is much smaller than that of bare Li at various current densities. Furthermore, the overpotentials of CC@Co-NCNTs@Li display a decreasing-stabilizing trend during long-term cycles at various current densities, which may be related to the lithium diffusion in the skeleton during electrochemical process. The lithium diffusion driven by electrochemical process into the void caused by previous lithium melting process, optimizing the integration of lithium and 3D skeleton and inducing uniform Li plating. This phenomenon was further analyzed by an observation of the cross sections of CC@Co-NCNTs@Li electrode before and after cycling, as shown in Figure S6. The cross-section of

CC@Co-NCNTs@Li at the initial state (Figure S6a), shows that the electrode is full of holes which results in irregular fluctuations at the cutting edge. However, after cycling for 200 h, the holes are almost filled with lithium, and the cross-section becomes flat and smooth. In addition, the thickness of the whole electrode decreases from 405 μm to 342 μm (Figure S6b). This demonstrates a good diffusion kinetic of lithium in the Co-anchored 3D skeleton which alleviates the lithium plating only on the surface of electrode and the formation of Li dendrites. Thus the superiority of the CC@Co-NCNTs skeleton is confirmed.

The rate performance of the CC@Co-NCNTs@Li electrode was shown in Fig. 5c. With the increase of the current density, the overpotential of CC@Co-NCNTs@Li electrode increases slightly and shows good regularity. When the current density drops back to 2 mA cm^{-2}, the electrode shows a lower overpotential of 2.1 mV (vs. initial 4.6 mV), which may be due to uniform lithium plating, optimized composite structure and stable SEI. Notably, these cheerful phenomenon are driven by the dynamic charge distribution, which guides the rapid and uniform lithium plating/stripping. In comparison, the overpotential distribution of bare Li electrode is not highly consistent with the changes in current density. The corresponding voltage hysteresis is still severe even when the current density returns to 2 mA cm^{-2}. In particular, the overpotential

fluctuates sharply when the current density exceeds 6 mA cm^{-2}. The rapid voltage rise may be due to the hindered lithium plating by the continuously thickened SEI film and the formation of dead lithium during the electroplating/stripping process, while the rapid voltage drop may be a short-circuit phenomenon caused by lithium dendrites through the penetrated separator [41,42].

The excellent reaction kinetics of the CC@Co-NCNTs@Li electrode was further demonstrated by the electrochemical impedance spectroscopy (EIS) (Figure S7). The equivalent circuit is shown in the inset of Figure S7a. The semicircles in the medium-high frequency region of the Nyquist diagram represent the interface resistance (R_f) at the SEI and the charge transfer resistance (R_{ct}) on the Li surface [43]. R_{ct} of the bare Li electrode before cycling (223 Ω) is significantly higher [44] than that of the CC@Co-NCNTs@Li electrode (53 Ω) in Figure. S7a. After the operation of 200 h, a smaller Rct (5 Ω) of bare Li electrode is obtained (Figure. S8b) due to the morphological changes on the surface of lithium during the repeated stripping/plating process[22]. The

CC@Co-NCNTs@Li electrode exhibits an ultra-small R_{ct} (3 Ω) due to the formation of a better electron/ion conduction network derived from the optimized integration of lithium and skeleton after cycling. In this condition , the electron aggregation area on the skeleton surface of CC@Co-NCNTs@Li electrode can be fully utilized , which brings the fastest interface charge transmission. Meanwhile, the CC@Co-NCNTs@Li electrode forms a more stable SEI film with better Li diffusion kinetics, maintaining the Li stripping/plating process with a low overpotential.

To better understand the Li stripping/plating behaviour in the CC@Co-NCNTs@Li electrodes, the structural evolution on the surfaces of bare lithium and CC@Co-NCNTs@Li electrode before and after 200 h cycles were analyzed by ex-situ SEM observation. The bare lithium in Fig. 6a has a relatively smooth surface only with a bit of nanoparticles and raised edges (3–6 μm). After 200 h cycling at a current density of 5 mA cm^{-2} with a capacity of 5 mAh cm^{-2}, numerous holes appear on the stripping surface of the bare lithium electrode and a clear dendritic
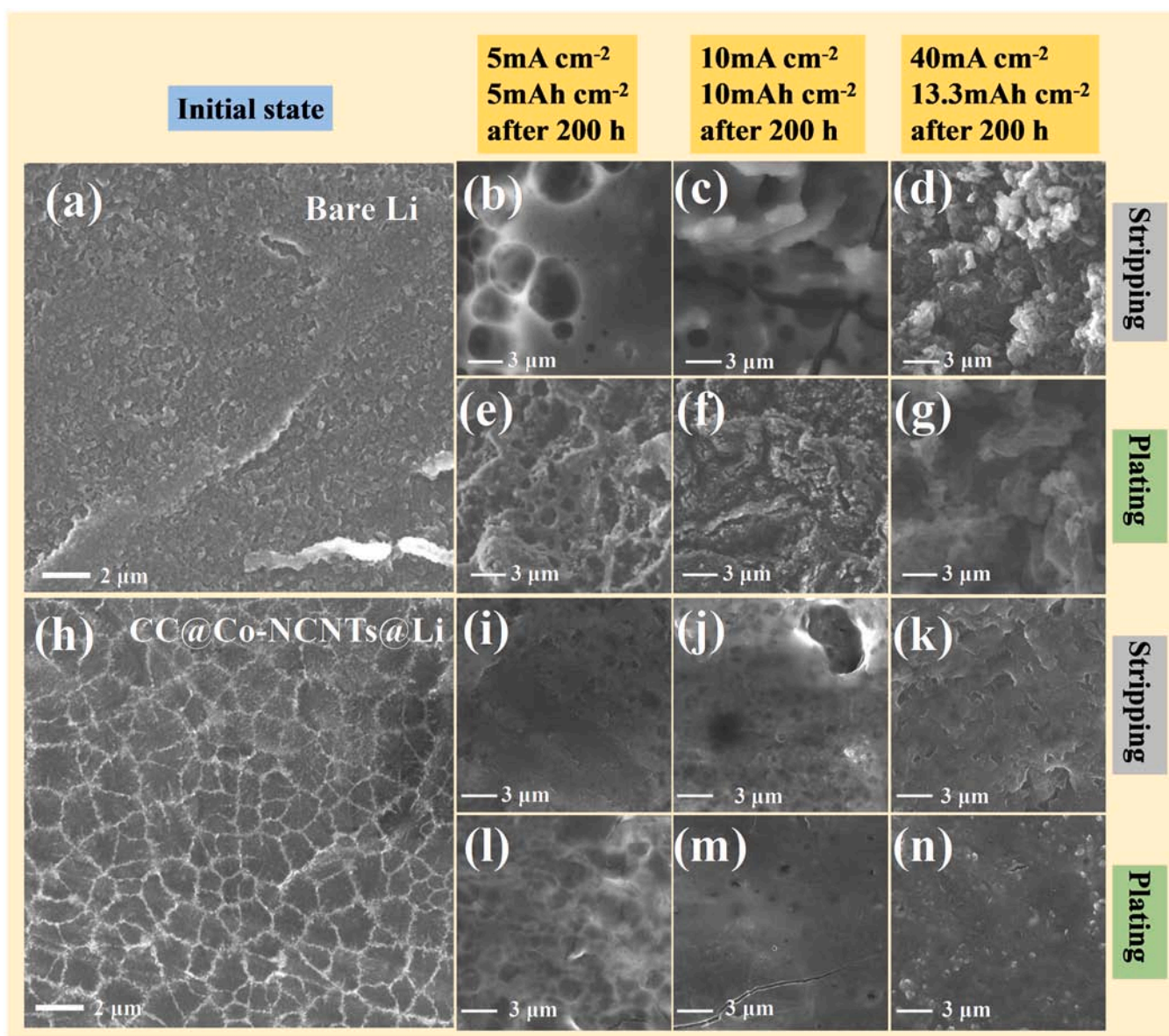
Fig. 6. SEM images of bare Li and CC@Co-NCNTs@Li before/after cycling. a) Surface morphology of bare Li before cycling. Surface morphology of bare Li after cycling at 5 mA cm^{-2} (5 mAh cm^{-2}), 10 mA cm^{-2} (10 mAh cm^{-2}) and 40 mA cm^{-2} (13.3 mAh cm^{-2}) current densities for 200 h, respectively. b, c, d) Stripping surface e, f, g) Plating surface. h) Surface morphology of CC@Co-NCNTs@Li before cycling. Surface morphology of CC@Co-NCNTs@Li after 200 h of current density cycling at 5 mA cm^{-2} (5 mAh cm^{-2}), 10 mA cm^{-2} (10 mAh cm^{-2}) and 40 mA cm^{-2} (13.3 mAh cm^{-2}) respectively i, j, k) Stripping surface l, m, n) Plating surface.

lithium form on the plating surface (Fig. 6 b, e). As the current density and stripping/plating capacity increase, obvious cracks and bumps appear on the stripping surface, while many stripe-like bumps grow on the plating side accompanied by cracks (Fig. 6c, f). Under condition of ultra-high current density, The stripping surface of bare lithium electrode even appears agglomerates and micron-sized particles instead of maintaining the original morphology, while the plating surface involves in larger bumps (5–7 μm) with new lumps (Fig. 6d, g). This phenomenon may be derived from Li dendrite growth and fracture in the continuous uneven plating process, which is easy to cause safety hazards in application. Conversely, the irregular shape of CC@Co-NCNTs@Li surface is obtained due to the collision of adjacent crystals as they grow during melting-recrystallization process (Fig. 6h). The CC@Co-NCNTs@Li electrodes exhibit a very smooth plating/peeling surface under all test conditions. Even after 200 h cycling at very high current density, only slight sunken morphology and sporadic nanoparticles appeared on the surface (Fig. 6i-n). The sunken morphology in Fig. 6j is caused by the lithium diffusion driven by electrochemical process into the void caused by previous lithium melting process. According to these results, the CC@Co-NCNTs@Li electrode with a function of dynamic charge regulation could effectively induce the uniform lithium plating, which is consistent with the results of calculations and experiment mentioned above.

In order to illustrate the lithium plating behavior modulated by the dynamic charge distribution on the surface of CC@Co-NCNTs skeleton, the complete Li plating process is shown in Fig. 7. According to DFT calculation results, the surface charge of Co clusters in the Co-NCNT model is transferred to NCNTs, which attracts lithium ions to adsorb preferentially on the surface of the nanotubes. When the electrons in this region are consumed by the reduction of lithium, the left Co cluster is equivalent to a positive center which shows homogeneous charge repulsion with subsequent lithium ions, thus resulting in lithium plating on the bare carbon nanotubes. This dynamic charge distribution always induces the anisotropic plating of lithium on the Co-NCNTs nanosheets, inhibiting the formation of lithium dendrite during Li plating process. As the plating process proceeds, the lithium tend to be deposited on the concave surfaces with negative curvature [45]. As a result, the sunken spaces between the nanosheets are preferentially filled with lithium until the complete encapsulation of CC@Co-NCNTs skeleton. In addition, the good electrical conductivity and lithophilicity of CC@Co-NCNTs contribute to the high-rate and dendrite-free lithium plating.

To demonstrate the feasibility of such a design in practical application, full batteries composed of the as-prepared CC@Co-NCNTs@Li anode and commercial LiFePO₄ (LFP) cathode were assembled for performance evaluation. As a comparison, bare Li anode and commercial LFP cathode were also assembled into batteries. The CC@Co-NCNTs@Li||LFP battery provides a reversible capacity of 143 mAh g^{-1} at the rate of 1 C, with a high capacity retention of 94.4 % after 500 cycles. For the bare Li||LFP battery, the reversible capacity is only 122 mAh g^{-1} at the same rate and the cyclic stability suffers irreversible damage after 150 cycles, following by severe capacity fade (Fig. 8a). According to the galvanostatic charge-discharge curves in Fig. 8b, the electrode polarization of the CC@Co-NCNTs@Li||LFP battery (101 mV) was significantly smaller than that of bare Li||LFP battery (164 mV), and the similar results were obtained at high current densities (Figure S8). In terms of coulombic efficiency (Fig. 8c), the initial value of CC@Co-NCNTs@Li||LFP battery is 91.33%, and quickly stabilize at > 99.9 % in the subsequent cycles. In practice, a CC@Co-NCNTs@Li||LFP battery could support the continuous operation of multiple LEDs, as displayed in the inset of Fig. 8c. The first coulombic efficiency of the Li||LFP battery is 88.78 % and fluctuates sharply after 150 cycles, demonstrating unstable cyclicity and low lithium utilization. The electrochemical impedance spectroscopy (EIS) in Fig. 8d demonstrates the smaller resistance of CC@Co-NCNTs@Li compared to bare Li in the full batteries. Fig. 8e compares the rate performance of the two batteries. Expectedly, the CC@Co-NCNTs@Li||LFP battery delivers high capacities at various current densities, while the bare Li||LFP battery shows low capacities, especially poor stability at high rate. It indicates that the formation of Li dendrites and dead Li on the bare Li anode not only increases the battery resistance but also reduces the Li utilization, resulting in poor performance of the bare Li||LFP battery. However, CC@Co-NCNTs@Li can effectively induce uniform Li plating, reduce polarization and avoid Li dendrites and dead Li formation. In practical application, the dynamic charge distribution on the anode surface of CC@Co-NCNTs@Li||LFP battery can effectively induce uniform Li plating, reduce polarization and avoid the formation of lithium dendrites and dead lithium, resulting in excellent practical performance.

4. Conclusion

In conclusion, a functional CC@Co-NCNTs@Li composite anode

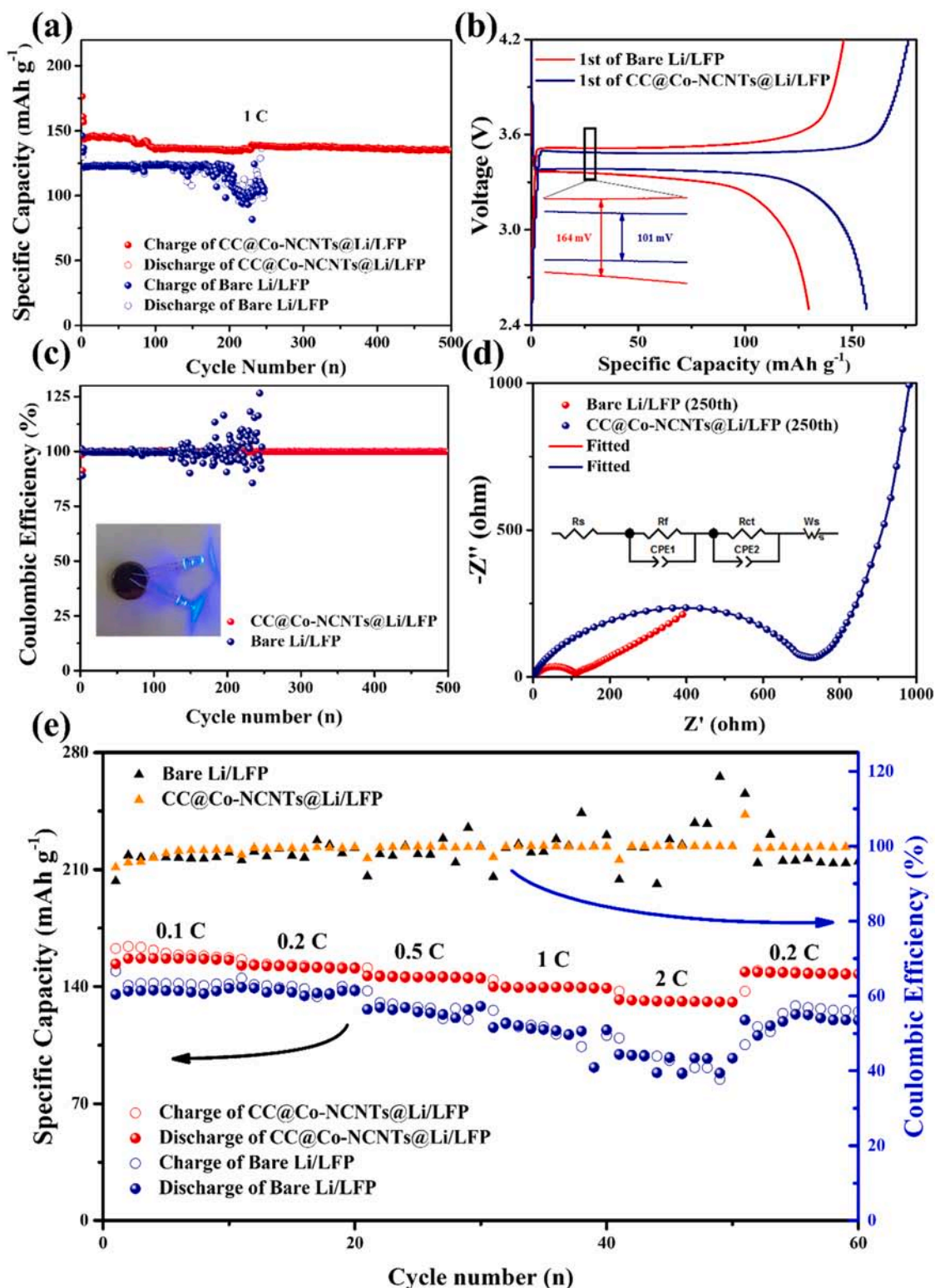**Fig. 7.** Three-dimensional schematic of the plating process of Li⁺ on CC@Co-NCNTs.

Fig. 8. Compared performances of CC@Co-NCNTs@Li||LFP battery and bare Li||LFP battery. a) Cyclic stability at 1 C (1 C = 170 mAh g^{-1}). b) Galvanostatic charge-discharge curves at 1 C. c) Coulomb efficiencies at 1 C. d) EIS curves after 250 cycles e) Rate performance at 0.1–2 C..

based on the 3D skeleton with good lithophilicity to induce the dendrite-free lithium plating. Thereinto, the interwoven carbon nanotubes and ingenious hierarchical structure provide a good conductive network and abundant nucleation sites for high-speed lithium plating, the dynamic charge distribution on the skeleton surface modulates the dendrite-free lithium plating, and the carbon fiber cloth as a substrate enables the

above functions. The symmetric cell with composite anode achieves a rare cyclic stability over 1300 h at a current density of 40 mAh cm^{-2}. The CC@Co-NCNTs@Li||LFP full battery delivers a reversible capacity of 135 mAh g^{-1} at a rate of 1 C after 500 cycles. This work provides valuable ideas for the development of a functional skeleton for lithium composite anodes that will greatly facilitate the development of lithium

metal batteries and lithium sulfur batteries.

CRediT authorship contribution statement

Wendi Zhang: Conceptualization, Methodology, Validation, Investigation, Writing – original draft, Writing – review & editing. **Qianxiao Fan**: Writing – review & editing, Formal analysis, Validation, Software. **Dongmei Zhang**: Writing – review & editing, Formal analysis, Validation, Software. **Lehao Liu**: Writing – review & editing. **Shen Liu**: Writing – review & editing, Validation. **Zhengyuan Fang**: Software, Methodology. **Wei Li**: Software, Methodology. **Xiaodan Li**: Resources, Supervision, Writing – review & editing. **Meicheng Li**: Funding acquisition, Resources, Supervision, Writing – review & editing.

Declaration of Competing Interest

The authors declare that they have no known competing financial interests or personal relationships that could have appeared to influence the work reported in this paper.

Data Availability

Data will be made available on request.

Acknowledgement

Appendix A. Supporting information

Supplementary data associated with this article can be found in the online version at doi:10.1016/j.nanoen.2022.107677.

References

[1] Y. Guo, H. Li, T. Zhai, Reviving lithium-metal anodes for next-generation high-energy batteries, Adv. Mater. 29 (2017) 1700007, https://doi.org/10.1002/adma.201700007.

[2] W. Xu, J. Wang, F. Ding, X. Chen, E. Nasybulin, Y. Zhang, J.-G. Zhang, Lithium metal an-odes for rechargeable batteries, Energy Environ. Sci. 7 (2014) 513–537, https://doi.org/10.1039/C3EE40795K.

[3] B. Wu, J. Lochala, T. Taverne, J. Xiao, The interplay between solid electrolyte interface (SEI) and dendritic lithium growth, Nano Energy 40 (2017) 34–41, https://doi.org/10.1016/j.nanoen.2017.08.005.

[4] C. Niu, H. Lee, S. Chen, Q. Li, J. Du, W. Xu, J.-G. Zhang, M.S. Whittingham, J. Xiao, J. Liu, High-energy lithium metal pouch cells with limited anode swelling and long stable cycles, Nat. Energy 4 (2019) 551–559, https://doi.org/10.1038/s41560-019-0390-6.

[5] Y. Liu, D. Lin, P.Y. Yuen, K. Liu, J. Xie, R.H. Dauskardt, Y. Cui, An artificial solid ele-ctrolyte interphase with high li-ion conductivity, mechanical Strength, and Flexibility for Stable Lithium Metal Anodes, Adv. Mater. 29 (2017) 1605531, https://doi.org/10.1002/adma.201605531.

[6] X.-B. Cheng, C. Yan, X. Chen, C. Guan, J.-Q. Huang, H.-J. Peng, R. Zhang, S.-T. Yang, Q. Zhang, Implantable solid electrolyte interphase in lithium-metal batteries, Chem 2 (2017) 258–270, https://doi.org/10.1016/j.chempr.2017.01.003.

[7] G. Sahu, Z. Lin, J. Li, Z. Liu, N. Dudney, C. Liang, Air-stable, high-conduction solid electr-olytes of arsenic-substituted Li4SnS4, Energy Environ. Sci. 7 (2014) 1053–1058, https://doi.org/10.1039/C3EE43357A.

[8] K. Liu, A. Pei, H.R. Lee, B. Kong, N. Liu, D. Lin, Y. Liu, C. Liu, et al., Lithium metal anodes with an adaptive "solid-liquid" interfacial protective layer, J. Am. Chem. Soc. 139 (2017) 4815–4820, https://doi.org/10.1021/jacs.6b13314.

[9] Z. Peng, X. Cao, P. Gao, H. Jia, X. Ren, S. Roy, Z. Li, Y. Zhu, W. Xie, D. Liu, Q. Li, D. Wang, W. Xu, J.-G. Zhang, High-power lithium metal batteries enabled by high-concentration acetonitrile-based electrolytes with vinylene carbonate additive, Adv. Funct. Mater. 30 (2020) 2001285, https://doi.org/10.1002/adfm.202001285.

[10] N. Piao, X. Ji, H. Xu, X. Fan, L. Chen, S. Liu, M.N. Garaga, S.G. Greenbaum, L. Wang, C. Wang, X. He, Countersolvent electrolytes for lithium-metal batteries, Adv. Energy Mater. 10 (2020) 1903568, https://doi.org/10.1002/aenm.201903568.

[11] J. Zheng, M.H. Engelhard, D. Mei, S. Jiao, B.J. Polzin, J.-G. Zhang, W. Xu, Electrolyte additive enabled fast charging and stable cycling lithium metal batteries, Nat. Energy 2 (2017) 17012, https://doi.org/10.1038/nenergy.2017.12.

[12] X.-B. Cheng, M.-Q. Zhao, C. Chen, A. Pentecost, K. Maleski, T. Mathis, X.-Q. Zhang, Q. Zhang, J. Jiang, Y. Gogotsi, Nanodiamonds suppress the growth of lithium dendrites, Nat. Commun. 8 (2017) 336, https://doi.org/10.1038/s41467-017-00519-2.

[13] M. Bai, K. Xie, B. Hong, K. Yuan, Z. Li, Z. Huang, C. Shen, Y. Lai, An artificial Li3PO4 solid electrolyte interphase layer to achieve petal-shaped deposition of lithium, Solid State Ion. 333 (2019) 101–104, https://doi.org/10.1016/j.ssi.2019.01.016.

[14] H. Lee, D.J. Lee, Y.-J. Kim, J.-K. Park, H.-T. Kim, A simple composite protective layer coating that enhances the cycling stability of lithium metal batteries, J. Power Sources 284 (2015) 103–108, https://doi.org/10.1016/j.jpowsour.2015.03.004.

[15] Q. Lu, X. Zou, R. Ran, W. Zhou, K. Liao, Z. Shao, An "electronegative" bifunctional coating layer: simultaneous regulation of polysulfide and Li-ion adsorption sites for long-cycling and "dendrite-free" Li–S batteries, J. Mater. Chem. A 7 (2019) 22463–22474, https://doi.org/10.1039/C9TA07999H.

[16] Q. Wang, C. Yang, J. Yang, K. Wu, L. Qi, H. Tang, Z. Zhang, W. Liu, H. Zhou, Stable Li metal anode with protected interface for high-performance Li metal batteries, Energy Storage Mater. 15 (2018) 249–256, https://doi.org/10.1016/j.ensm.2018.04.030.

[17] K. Liao, S. Wu, X. Mu, Q. Lu, M. Han, P. He, Z. Shao, H. Zhou, Developing a "water-defendable" and "dendrite-free" lithium-metal anode using a simple and promising GeCl4 pretreatment method, Adv. Mater. 30 (2018) 1705711, https://doi.org/10.1002/adma.201705711.

[18] R. Zhang, X. Chen, X. Shen, X.-Q. Zhang, X.-R. Chen, X.-B. Cheng, C. Yan, C.-Z. Zhao, Q. Zhang, Coralloid carbon fiber-based composite lithium anode for robust lithium metal batteries, Joule 2 (2018) 764–777, https://doi.org/10.1016/j.joule.2018.02.001.

[19] Y. Wang, Z. Wang, D. Lei, W. Lv, Q. Zhao, B. Ni, Y. Liu, B. Li, F. Kang, Y.-B. He, Spherical Li deposited inside 3D Cu skeleton as anode with ultrastable performance, ACS Appl. Mater. Interfaces 10 (2018) 20244–20249, https://doi.org/10.1021/acsami.8b04881.

[20] Q. Yun, Y.-B. He, W. Lv, Y. Zhao, B. Li, F. Kang, Q.-H. Yang, Chemical dealloying derived 3D porous current collector for Li metal anodes, Adv. Mater. 28 (2016) 6932–6939, https://doi.org/10.1002/adma.201601409.

[21] L.-L. Lu, J. Ge, J.-N. Yang, S.-M. Chen, H.-B. Yao, F. Zhou, S.-H. Yu, Free-standing copper nanowire network current collector for improving lithium anode performance, Nano Lett. 16 (2016) 4431–4437, https://doi.org/10.1021/acs.nanolett.6b01581.

[22] S.-S. Chi, Y. Liu, W.-L. Song, L.-Z. Fan, Q. Zhang, Prestoring lithium into stable 3D nickel foam host as dendrite-free lithium metal anode, Adv. Funct. Mater. 27 (2017) 1700348, https://doi.org/10.1002/adfm.201700348.

[23] G. Huang, J. Han, F. Zhang, Z. Wang, H. Kashani, K. Watanabe, M. Chen, Lithiophilic 3D nanoporous nitrogen-doped graphene for dendrite-free and ultrahigh-rate lithium-metal anodes, Adv. Mater. 31 (2019) 1805334, https://doi.org/10.1002/adma.201805334.

[24] P. Shi, T. Li, R. Zhang, X. Shen, X.-B. Cheng, R. Xu, J.-Q. Huang, X.-R. Chen, H. Liu, Q. Zhang, Lithiophilic LiC6 layers on carbon hosts enabling stable Li metal anode in working batteries, Adv. Mater. 31 (2019) 1807131, https://doi.org/10.1002/adma.201807131.

[25] R. Zhang, X.-R. Chen, X. Chen, X.-B. Cheng, X.-Q. Zhang, C. Yan, Q. Zhang, Lithiophilic sites in doped graphene guide uniform lithium nucleation for dendrite-free lithium metal anodes, Angew. Chem. Int. Ed. 56 (2017) 7764–7768, https://doi.org/10.1002/anie.201702099.

[26] Q. Song, H. Yan, K. Liu, K. Xie, W. Li, W. Gai, G. Chen, H. Li, C. Shen, Q. Fu, S. Zhang, L. Zhang, B. Wei, Vertically grown edge-rich graphene nanosheets for spatial control of Li nucleation, Adv. Energy Mater. 8 (2018) 1800564, https://doi.org/10.1002/aenm.201800564.

[27] K. Li, Z. Hu, J. Ma, S. Chen, D. Mu, J. Zhang, A 3D and stable lithium anode for high-performance lithium–iodine batteries, Adv. Mater. 31 (2019) 1902399, https://doi.org/10.1002/adma.201902399.

[28] X. Chen, X.-R. Chen, T.-Z. Hou, B.-Q. Li, X.-B. Cheng, R. Zhang, Q. Zhang, Lithiophilicity chemistry of heteroatom-doped carbon to guide uniform lithium nucleation in lithium metal anodes, Sci. Adv. 5 (2019) eaau7728, https://doi.org/10.1126/sciadv.aau7728.

[29] Y. Liu, D. Lin, Z. Liang, J. Zhao, K. Yan, Y. Cui, Lithium-coated polymeric matrix as a minimum volume-change and dendrite-free lithium metal anode, Nat. Commun. 7 (2016) 10992, https://doi.org/10.1038/ncomms10992.

[30] R. Zhang, S. Wen, N. Wang, K. Qin, E. Liu, C. Shi, N. Zhao, N-doped graphene modified 3D porous Cu current collector toward microscale homogeneous Li deposition for Li metal anodes, Adv. Energy Mater. 8 (2018) 1800914, https://doi.org/10.1002/aenm.201800914.

[31] J.S. Meng, C.J. Niu, L.H. Xu, J.T. Li, X. Liu, X.P. Wang, Y.Z. Wu, X.M. Xu, W. Y. Chen, Q. Li, Z.Z. Zhu, D.Y. Zhao, L.Q. Mai, General oriented formation of carbon

nanotubes from metal-organic frameworks, J. Am. Chem. Soc. 139 (2017) 8212–8221, https://doi.org/10.1021/jacs.7b01942.

[32] W. Zhang, Z. Fang, H. Song, M. Lu, M. Li, D. Wei, X. Li, Binary metal oxide anchored into dense N-doped CNTs arrays: concerted pseudocapacitance and diffusion behavior for long-cyclic Li-ion half/full batteries, Appl. Surf. Sci. (2021), 151618, https://doi.org/10.1016/j.apsusc.2021.151618.

[33] P. Kumar, E. Vahidzadeh, U.K. Thakur, P. Kar, K.M. Alam, A. Goswami, N. Mahdi, K. Cui, G.M. Bernard, V.K. Michaelis, K. Shankar, C3N5: a low bandgap semiconductor containing an Azo-linked carbon nitride framework for photocatalytic, photovoltaic and adsorbent applications, J. Am. Chem. Soc. 141 (2019) 5415–5436, https://doi.org/10.1021/jacs.9b00144.

[34] H. Li, X. Qian, C. Xu, S. Huang, C. Zhu, X. Jiang, L. Shao, L. Hou, Hierarchical porous Co9S8/Nitrogen-doped carbon@MoS2 polyhedrons as pH universal electrocatalysts for highly efficient hydrogen evolution reaction, ACS Appl. Mater. Interfaces 9 (2017) 28394–28405, https://doi.org/10.1021/acsami.7b06384.

[35] E. Riedo, F. Comin, J. Chevrier, F. Schmithusen, S. Decossas, M. Sancrotti, Structural properties and surface morphology of laser-deposited amorphous carbon and carbon nitride films, Surf. Coat. Tech. 125 (2000) 124–128, https://doi.org/10.1016/s0257-8972(99)00591-5.

[36] X. Lu, D. Wang, L. Ge, L. Xiao, H. Zhang, L. Liu, J. Zhang, M. An, P. Yang, Enriched graphitic N in nitrogen-doped graphene as a superior metal-free electrocatalyst for the oxygen reduction reaction, New. J. Chem. 42 (2018) 19665–19670, https://doi.org/10.1039/C8NJ04857F.

[37] Y. Zhao, Q. Lai, Y. Wang, J. Zhu, Y. Liang, Interconnected hierarchically porous Fe, N-codoped carbon nanofibers as efficient oxygen reduction catalysts for Zn–air batteries, ACS Appl. Mater. Interfaces 9 (2017) 16178–16186, https://doi.org/10.1021/acsami.7b01712.

[38] L. Yang, H. Li, Y. Yu, Y. Wu, L. Zhang, Assembled 3D MOF on 2D nanosheets for self-boosting catalytic synthesis of n-doped carbon nanotube encapsulated metallic

Co electrocat-alysts for overall water splitting, Appl. Catal. B-Environ. 271 (2020), 118939, https://doi.org/10.1016/j.apcatb.2020.118939.

[39] J. Sun, W. Xu, C. Lv, L. Zhang, M. Shakouri, Y. Peng, Q. Wang, X. Yang, D. Yuan, M. Huang, Y. Hu, D. Yang, L. Zhang, Co/MoN hetero-interface nanoflake array with enhanced water dissociation capability achieves the Pt-like hydrogen evolution catalytic performance, Appl. Catal. B-Environ. 286 (2021), 119882, https://doi.org/10.1016/j.apcatb.2021.119882.

[40] Z.Y. Wang, Z.X. Lu, W. Guo, Q. Luo, Y.H. Yin, X.B. Liu, Y.S. Li, B.Y. Xia, Z.P. Wu, A. Dendrite-Free Lithium/Carbon, Nanotube hybrid for lithium-metal batteries, Adv. Mater. 33 (2021) 2006702, https://doi.org/10.1002/adma.202006702.

[41] P. Shi, X.-B. Cheng, T. Li, R. Zhang, H. Liu, C. Yan, X.-Q. Zhang, J.-Q. Huang, Q. Zhang, Electrochemical diagram of an ultrathin lithium metal anode in pouch cells, Adv. Mater. 31 (2019) 1902785, https://doi.org/10.1002/adma.201902785.

[42] F. Liu, R. Xu, Z. Hu, S. Ye, S. Zeng, Y. Yao, S. Li, Y. Yu, Regulating lithium nucleation via CNTs modifying carbon cloth film for stable Li metal anode, Small 15 (2019) 1803734, https://doi.org/10.1002/smll.201803734.

[43] N.A. Canas, K. Hirose, B. Pascucci, N. Wagner, K.A. Friedrich, R. Hiesgen, Investigations of lithium-sulfur batteries using electrochemical impedance spectroscopy, Electro Acta 97 (2013) 42–51, https://doi.org/10.1016/j.electacta.2013.02.101.

[44] D. Lin, Y. Liu, Z. Liang, H.-W. Lee, J. Sun, H. Wang, K. Yan, J. Xie, Y. Cui, Layered reduced graphene oxide with nanoscale interlayer gaps as a stable host for lithium metal anodes, Nat. Nanotechnol. 11 (2016) 626–632, https://doi.org/10.1038/nnano.2016.32.

[45] W. Ye, L. Wang, Y. Yin, X. Fan, Y. Cheng, H. Gao, H. Zhang, Q. Zhang, G. Luo, M.-S. Wang, Lithium storage in bowl-like carbon: the effect of surface curvature and space Ge-ometry on Li metal deposition, ACS Energy Lett. 6 (2021) 2145–2152, https://doi.org/10.1021/acsenergylett.1c00456.